nature chemistry

Article

https://doi.org/10.1038/s41557-023-01225-x

Efficient photon upconversion enabled by strong coupling between silicon quantum dots and anthracene

In the format provided by the authors and unedited

Supplementary information for:

Efficient photon upconversion enabled by strong coupling between silicon quantum dots and anthracene

Kefu Wang[1#], R. Peyton Cline[2#], Joseph Schwan[3#], Jacob M. Strain[4], Sean T. Roberts[4*], Lorenzo Mangolini[3*], Joel D. Eaves[2*], Ming Lee Tang[1*]

[1]*Department of Chemistry, University of Utah, Salt Lake City, USA; University of California, Riverside, Riverside, USA.*

[2]*Department of Chemistry, University of Colorado Boulder, Boulder, USA.*

[3]*Department of Mechanical Engineering, University of California Riverside, Riverside, USA.*

[4]*Department of Chemistry, The University of Texas at Austin, Austin, USA*

[#]*These authors contributed equally*

[*]*E-mail address: roberts@cm.utexas.edu; lmangolini@engr.ucr.edu; Joel.Eaves@colorado.edu; minglee.tang@utah.edu*

Contents

1. Instrumentation

Absorption spectra were recorded on a Cary 5000 UV-Vis absorption spectrophotometer. Photoluminescence (photon upconversion, power dependence) spectra were recorded on a Maya 2000-Pro Spectrometer (Ocean Optics Inc.) following excitation by continuous wave (CW) solid-state lasers (375 nm: OBIS LX 50 mW, Coherent Inc.; 488 nm: OBIS LX 75 mW, Coherent Inc.; 532 nm: Sapphire SF 532, Coherent Inc.). Neutral density filters (Thorlabs) were used to tune the power of the excitation source without changing its beam size. Semrock notch filters were used to remove the excitation light following the sample. Laser power was measured using a benchtop optical power and energy meter (2936R, Newport Corp.) and silicon wand detector head (818-ST2/DB, Newport Corp.).

Transmission electron microscopy (TEM) imaging was taken with a Tecnai12 operating at 120 kV. Samples were deposited on a thin-film carbon grid with copper supports via drop-casting while suspended in a chloroform solution.

X-ray diffraction (XRD) measurements were taken using a PANalytical Empyrean X-Ray system that used Cu Kα radiation with a wavelength of 1.54 Å. Dry unfunctionalized samples were placed on top of a silicon zero-diffraction plate and scanned without sample rotation.

Nuclear magnetic resonance (NMR) spectra were recorded on a Bruker AVANCE NEO 400 MHz NMR spectrometer at room temperature. ^{1}H chemical shifts (δ) are reported in parts per million with a residual solvent ($CDCl_3$) peak as an internal standard.

All transient absorption (TA) measurements with the exception of data highlighted in **Supplementary Figure 7** were conducted using an enVISion spectrometer from Magnitude Instruments that employed a 532 nm excitation laser. The repetition rate of the excitation laser was varied from 1 kHz to 19 kHz depending on the size of the delay time window scanned, with lower repetition rates used for longer time windows. TA spectra highlighted in **Figures 4** and **5** of the main text and **Supplementary Figures 5** and **6** were recorded using a 10 kHz repetition rate and a pump fluence of 150 $\mu J/cm^2$. The instrument response function for these measurements was found to give a time resolution of 4.2 ns. Higher time resolution TA experiments with an instrument response of ~1.6 ns (**Supplementary Figure 7**) were performed using 532 nm pump pulses generated by a frequency-doubled Q-switched Nd:YAG laser (Alphalas Pulselas-A, < 1 ns, 8.7 μJ). Supercontinuum probe pulses were produced by focusing the output of a Ti:sapphire amplifier operating at 804 nm (Coherent Duo Legend Elite, 3 kHz, 4.5 mJ) into a flowing liquid cell filled with D_2O (Starna). A digital delay generator (Stanford Research Systems DG535) was used to synchronize the operation of the pump and probe lasers and to vary their time of arrival at the sample. A silicon CCD (Princeton Instruments PyLoN 100-BR) interfaced with a 500 mm Czerny-Turner spectrometer (Acton Instruments Spectra Pro 2556) was used to detect pump-induced changes in the transmission of the probe through the sample. All silicon QD samples used for TA measurements were prepared in a nitrogen glove box and placed into sealed cuvettes.

2. Sample Preparation

2.1 Materials

9-vinyl anthracene (9VA, 97%) and 9,10-diphenylanthracene (DPA, 98%) were purchased from TCI America. Platinum octaethylporphyrin (PtOEP, 98%) used for triplet sensitization experiments and 2,2'-Azobis(2-methylpropionitrile) (AIBN) came from Sigma Aldrich. Deuterated chloroform ($CDCl_3$, 99.8%) was obtained from Cambridge Isotope Laboratories, Inc. Toluene was purchased from Fisher and dried and degassed with a JC Meyer solvent purification system. Dried methanol was procured from Sigma Aldrich and degassed before moving it into a glove box. Mesitylene (98%) was likewise obtained from Sigma Aldrich and was dried with molecular sieves. All other chemicals were used as received.

2.2 Synthesis of 9-acetylene anthracene (9AA)

9-acetylene anthracene (9AA) was synthesized from 9-bromoanthracene according to Nierth et al.[1] NMR spectra of synthesized 9AA were found to be consistent with this prior published report.

2.3 Synthesis and Surface Functionalization of Silicon Quantum Dots (Si QDs)

Si QDs partially functionalized with 1-dodecene (Si:dodecane) were synthesized using a non-thermal plasma reactor following the approached described in Refs. 2 and 3. In this process, Si QDs are first nucleated and grown in a low-temperature plasma using silane gas (SiH_4) as a precursor. Hydrogen gas saturated with 1-dodecene vapor is introduce in the plasma afterglow to graft alkyl chains to QDs. The flow rate of the saturated hydrogen gas was optimized to ensure that the QDs form a stable colloidal dispersion in mesitylene, all while having a sufficient fraction of their surface still available for additional modification. After synthesis, these QDs were transferred to a glovebox under a nitrogen environment and dissolved in toluene. The resulting concentrated Si:dodecane solution was then diluted with mesitylene until its optical density at 488 nm was ~1.2 in a 1 cm pathlength cuvette, after which it was heated at 180 ºC for 1.5 hours to reduce Si QD surface defects.

Prior studies that produced Si QDs using the non-thermal plasma synthesis method we employ have resulted in an output material with a mean diameter of 3 nm and standard deviation of 0.5 nm, as assessed by transmission electron microscopy (TEM).[4] We have performed similar TEM measurements on Si QD samples used in this study and found they are consistent with this value (**Supplementary Figure 1a, inset**). We also note emission spectra of the Si QDs we employ (**Supplementary Figure 1b**) show a peak at 742 nm (1.67 eV) that corresponds to an average Si QD size of 3.1 nm on the basis of published Si QD sizing curves.[5] Powder x-ray diffraction (XRD) measurements (**Supplementary Figure 1a**) indicate the QDs we employ are crystalline as peaks appear that are consistent with the (111), (220), and (311) planes bulk silicon. However, we note that a Scherrer analysis applied to the (111) peak is suggestive of crystalline Si QDs with a core diameter of only 2.4 nm rather than 3.1 nm. We have previously noted a discrepancy between sizes predicted by emission spectroscopy and XRD measurements.[6] This discrepancy suggests the Si QDs possess crystalline interiors that are surrounded by a partially disordered outer layer.

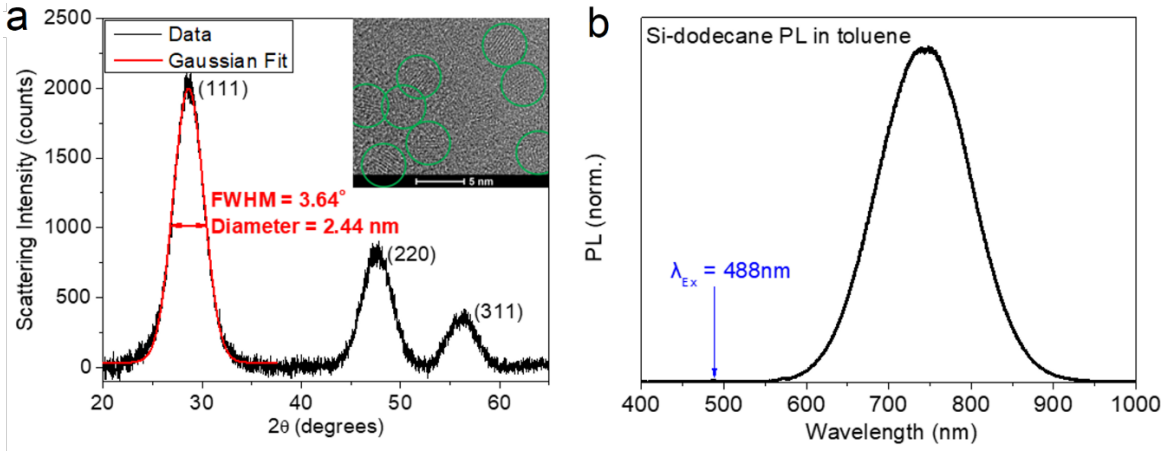

Supplementary Figure 1: (a) Powder XRD pattern of Si:dodecane QDs. (Inset) TEM image of Si:dodecane QDs. (b) Emission spectra ($\lambda_{Ex} = 488$ nm) of Si:dodecane QDs dissolved in toluene.

To prepare Si QDs with different anthracene surface concentrations, varying amounts of 9VA and 9AA were used during Si QD hydrosilylation (**Supplementary Table 1**). We found that these in-flight functionalized Si QDs were amenable to thermal hydrosilylation at 180 ºC using 9VA, but not 9AA as uncontrolled ligand polymerization occurred. We addressed this by performing radical initiated hydrosilylation using 2,2'-azobis(2-methylpropionitrile) (AIBN) for both 9VA and 9AA at 60 ºC (**Supplementary Figure 2**). All precursors needed to functionalize Si QDs via radical-initiated hydrosilylation were added to a 20 mL vial with a Teflon cap, which was then sealed and heated to 60 ºC overnight while undergoing constant stirring. This induces silicon hydrosilylation with 9VA and 9AA, thus forming 9-ethyl anthracene (9EA) attached to Si QDs (Si QD-C-C-anthracene, labeled as Si:9EA) and 9-vinyl anthracene (9VA) attached to Si QDs (Si QD-C=C-anthracene, labeled as Si:9VA), respectively. After

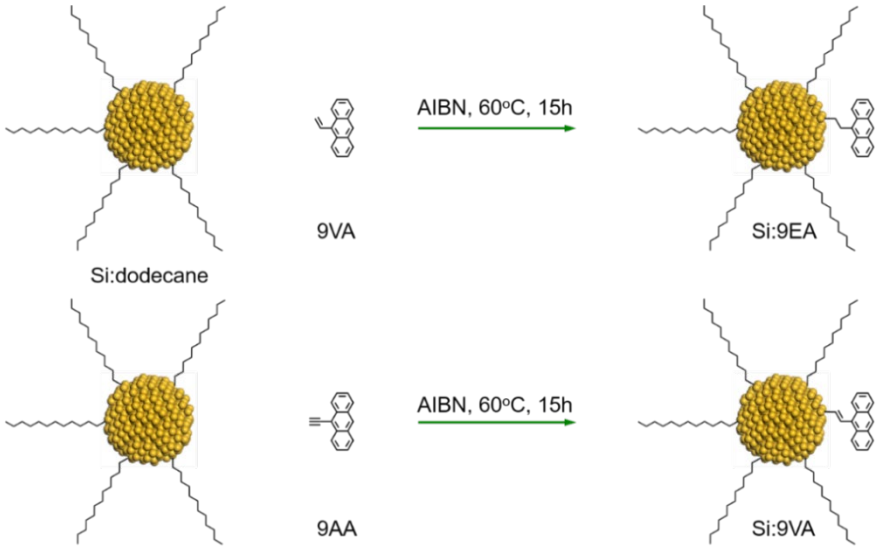

Supplementary Figure 2: Schematic illustration of Si QD hydrosilylation with 9VA and 9AA.

the reaction, methanol was added to the clear yellow mixture (methanol:mixture = 2:1 by volume) to precipitate out the QDs by centrifuging at 12,000 rpm (15,777 ×g) for 30 mins. The precipitated QDs are then redispersed in 1.5 mL of toluene, followed by addition of 3 mL of methanol and centrifuged at 12,000 rpm (15,777 ×g) for 20 mins again. This cleaning procedure was repeated three times and the final Si:9EA or Si:9VA samples were redispersed in toluene for future use.

For photon upconversion measurements, Si:9EA solutions were diluted with toluene to give them an optical density of ~0.1 at 488 nm in a 1 cm pathlength cuvette. At that point, 9,10-diphenylanthacene (DPA) was added to the Si:9EA solution to give a final DPA concentration of 5.2 mM. The resulting mixture was transferred into a 10 mm × 10 mm quartz cuvette sealed with an air-tight Teflon cap in a glovebox before taking out for testing. The same procedure was applied to the preparation of Si:9VA with 2,5,8,11-tetra-tert-butylperylene (*t*Bu$_4$P) emitters (5.2 mM).

	Si QDs (OD_{488} = 1.2)	9VA or 9AA (1 mg/mL)	AIBN (0.1 mg/mL)
Sample 1	200 µL	8 µL (8 µg)	6 µL
Sample 2	200 µL	31 µ (31 µg)	25 µL
Sample 3	200 µL	125 µL (125 µg)	100 µL
Sample 4	200 µL	500 µL (500 µg)	400 µL

Supplementary Table 1: Parameters used to prepare Si QDs with different surface ligand content via hydrosilylation in dry and degassed mesitylene. 2.000 mL of mesitylene was used for each reaction.

3. Characterization

3.1. Quantification of Number of Surface-bound Anthracene Molecules

The average number of anthracene molecules that bind to the surfaces of Si:9VA and Si:9EA was assessed using absorption spectroscopy. As highlighted in **Figure 1** of the main text, absorption spectra of Si:9VA and Si:9EA show distinct vibronic progressions in the range of 340 – 460 nm that arise from surface-bound anthracene molecules. The amplitude of these features can be obtained by subtracting the absorption spectrum of Si:dodecane from that of Si:9VA and Si:9EA samples. Prior to subtraction, to normalize for variations in the Si QD concentration of each sample, the Si:dodecane spectrum was scaled to match that of Si:9EA and Si:9VA in the spectral region between 550 – 700 nm wherein neither 9EA nor 9VA absorbs

light. For Si:9EA, we can compare this background subtracted spectrum to reported molar extinction coefficients for 9-methylanthracene (9MA) to determine the concentration of surface-bound 9EA molecules in solution while the Si QD concentration can be determined using reported extinction spectra. This yields the following expression for $\langle N_{9EA} \rangle$, the average number of surface-bound 9EA molecules:

$$\langle N_{9EA} \rangle = \frac{[9EA]}{[Si\ NC]} = \frac{abs_{Si:9EA,395nm} - abs_{Si:dodecane,395nm} \frac{\langle abs_{Si:9EA} \rangle}{\langle abs_{Si:C12} \rangle}}{\varepsilon_{9MA,389nm}} \Big/ \frac{abs_{Si:9EA,488nm}}{\varepsilon_{Si\ NC,488nm}} \quad (1)$$

Here, $\langle abs_{Si:9EA} \rangle / \langle abs_{Si:C12} \rangle$ denotes to the normalization value used to match absorption spectra of Si:9EA and Si:dodecane across the 550 – 700 nm spectral range, $\varepsilon_{Si\ NC,488nm}$ is the molar extinction coefficient of the ~3.1 nm diameter Si QDs we employ at 488 nm (10,000 $M^{-1}cm^{-1}$),[7] and $\varepsilon_{9MA,389nm}$ is the molar extinction coefficient of 9-methylanthracene at 389 nm (8,413 $M^{-1}cm^{-1}$),[8] which corresponds to the maximum of its 0-0 vibronic transition. Note, in comparing the extinction spectra of 9MA to background subtracted spectra of Si:9EA, we account for a 6 nm red shift in the absorption maxima of the latter's 0-0 transition that results from the difference in the dielectric environments felt by 9MA molecules dissolved in toluene and 9EA molecules bound to the surface of Si QDs.[8]

A similar calculation to determine $\langle N_{9VA} \rangle$, the number of anthracene molecules attached to the surface of Si:9VA, was performed using a measured molar extinction coefficient of 9VA of 6,900 $M^{-1}cm^{-1}$ at 389 nm. We note that due to strong coupling between Si QDs and 9VA molecules, absorption spectra of surface-bound 9VA molecules are significantly broadened relative that of 9VA molecules dispersed in solution (**Figure 1B**, **inset**). This will lead to a systematic underestimation of $\langle N_{9VA} \rangle$. However, as we are only interested in how the photoexcited dynamics and photon upconversion efficiency of Si:9VA change with increasing $\langle N_{9VA} \rangle$ and not the explicit dependence of these properties on a specific value of $\langle N_{9VA} \rangle$, this systematic underestimate does not impact any of the conclusions we draw in the main text.

Si:9EA	9VA / μg	2	8	31	125	500	> 500
	$\langle N_{9EA} \rangle$	NA	1.3	3.0	5.4	6.7	> 7
Si:9VA	9AA / μg	2	8	31	125	500	> 500
	$\langle N_{9EA} \rangle$	0.9	1.8	2.9	5.3	5.9	7.3

Supplementary Table 2: The average number of attached 9EA or 9VA per Si QD, $\langle N_{9EA} \rangle$ or $\langle N_{9VA} \rangle$, with respect to different precursor loadings for the Si QD hydrosilylation process.

3.2. Photon Upconversion Quantum Efficiency Measurements

Photon upconversion measurements were performed using 488 nm and 532 nm OBIS Coherent lasers as excitation sources and an Ocean Optics Maya 2000 Pro spectrometer for detection of upconverted light. Emitted photoluminescence (PL) was filtered through a ThorLabs notch filter before being received by the spectrometer to remove scattered excitation light. For each upconversion measurement, the system was calibrated using Rhodamine 6G (R6G) dissolved in ethanol as an emission reference (PLQY = 95%). We note that the spectral response of our emission setup was found to be flat across the visible spectral range using a calibrated light source, which allowed us to use R6G as an emission standard even though its emission spectrum does not overlap with that of DPA or *t*Bu_4P. The upconversion photon quantum yield (UCQY) was determined using the following expression:

$$\phi_{UC} = 2 \times \phi_{ref} \times \frac{photons\ absorbed\ by\ reference}{photons\ absorbed\ by\ upconversion\ solution} \times \frac{upconversion\ PL}{reference\ PL} \quad (2a)$$

$$= 2 \times \phi_{R6G} \times \frac{1 - 10^{-OD_{R6G}}}{1 - 10^{-OD_{Si\ QD}}} \times \frac{n^2_{Emitter}}{n^2_{R6G}} \times \frac{[Area]_{Emitter}}{[Area]_{R6G}} \quad (2b)$$

where ϕ_{ref} is the PLQY of R6G, $n_{Emitter}$ and n_{R6G} are the refractive indices of the solvents for the upconversion and R6G reference solutions (toluene and ethanol, respectively), OD_{R6G} and $OD_{Si\ QD}$ denote the absorbance of Si QDs and R6G at the laser excitation wavelength, and $[Area]_{Emitter}$ and $[Area]_{R6G}$ are the integrated areas of the fluorescence peaks of the emitter (either DPA or *t*Bu$_4$P) and R6G, respectively. Note, this expression includes a factor of 2 to normalize the maximum UCQY that is achievable to a value of 100%.

We also note that the presence of surface-bound anthracene molecules are critical to obtaining photon upconversion. Upconversion measurements were performed using Si:dodecane particles that had been paired with 5.2 mM DPA emitters, but this resulted in an UCQY of only 0.18%. This was expected since dodecane presents a formidable tunneling barrier that hinders triplet energy transfer from Si QDs to DPA.

3.3. Correcting Photon Upconversion Efficiency Yields to Account for Reabsorption of Emitted Light

For photon upconversion measurements, a high emitter concentration can lead to a strong reabsorption of upconverted light by emitter molecules in solution (inner filter effect), thereby leading to an underestimate of the UCQY if one was to simply compute this value using the intensity of emission bands recorded in an experiment. To correct for the inner filter effect, we follow a procedure outlined by Olesund et al.[9] In this procedure, we start by measuring emission spectra of upconversion emitters (DPA & *t*Bu$_4$P) by directly exciting these emitters in low concentration solutions wherein negligible reabsorption of emitted light occurs (**Supplementary Figure 3**). Negligible reabsorption in these low concentration reference solutions was confirmed by verifying a lack of dependence of their emission lineshape on emitter concentration. Emission spectra measured from upconversion samples were then normalized to these low-concentration reference spectra by matching spectra along their long-wavelength edges wherein emitters show no appreciable absorption. This allowed us to compute the ratio of the integrated area of the photon upconversion lineshape and the intrinsic emission lineshape of the emitter, which was then used to scale measured UCQYs to account for the reabsorption of emitted light. Taking into account the inner filter effect, UCQYs of Si:9EA:DPA and Si:9VA:*t*Bu$_4$P systems were computed to adopt maximum values of 15.8% and 17.2%, respectively, following optimization of the surface concentration of 9EA and 9VA.

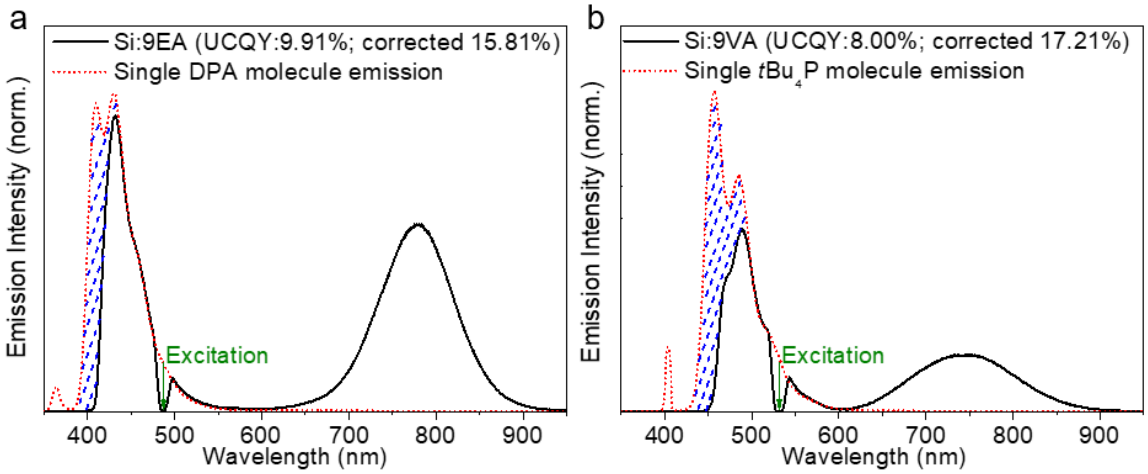

Supplementary Figure 3: (a) PL spectra of Si:9EA:DPA ($\langle N_{9EA} \rangle$ = 2.98, black solid line, 5.2 mM DPA as emitter, excited at 488 nm) and low-concentration DPA (red dashed line, excited at 365 nm). (b) PL spectra of Si:9VA:*t*Bu$_4$P ($\langle N_{9VA} \rangle$ = 2.87, black solid line, 5.2 mM *t*Bu$_4$P as emitter, excited at 532 nm) and low-concentration *t*Bu$_4$P (2 μM, red dashed line, excited at 405 nm). The broad emission band that appears between 660 and 900 nm corresponds to residual emission from Si QD bandedge states.[8] This emission is highly quenched by attachment of either 9EA or 9VA.

3.4. Dependence of Photon Upconversion Emission on Excitation Density

For photon upconversion measurements, the excitation density threshold is an important parameter that

characterizes the performance of the upconversion system. Above the threshold, triplet fusion ceases to be rate-limiting as the steady-state population of emitters in excited spin-triplet states is sufficiently high that every excited emitter can undergo triplet fusion with an excited partner before their triplet excitations decay to the ground state.[10] In this regime, photon upconversion operates with its maximum quantum efficiency as only decay processes intrinsic to each participating species (Si QD, transmitter, and emitter) compete with upconversion. The point at which this threshold is reached is signaled by a change in the dependence of the intensity of upconverted light from a quadratic dependence on excitation density, and hence triplet concentration, to a linear dependence that is independent of triplet concentration.

Supplementary Figure 4a plots the dependence of the upconverted emission produced by DPA when paired with Si:9VA on the intensity of a 488 nm excitation source while **Supplementary Figure 4b** plots the dependence of upconverted emission generated by *t*Bu4P when paired with Si:9VA on the intensity of a 532 nm excitation source. We find both systems exhibit low excitation density thresholds (1.5 W/cm^2 for Si:9EA and 0.5 W/cm^2 for Si:9VA). To the best of our knowledge, the excitation density threshold for Si:9VA is the lowest yet reported for Si QD-based upconversion systems.

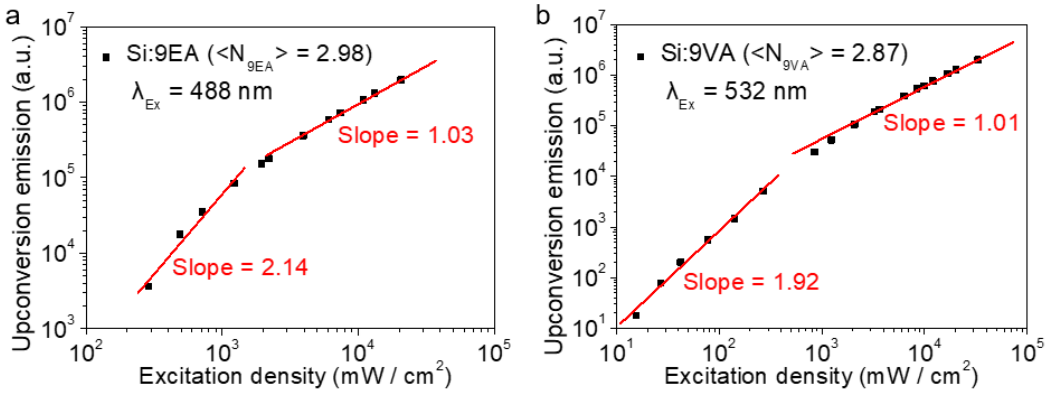

Supplementary Figure 4: Log-log plots of the upconverted emission intensity of (a) Si:9EA ($\langle N_{9EA} \rangle$ = 2.98, DPA as emitter) versus laser excitation (488 nm) power and (b) the upconverted emission intensity of Si:9VA ($\langle N_{9VA} \rangle$ = 2.87, *t*Bu$_4$P as emitter) versus laser excitation (532 nm) power.

3.5. Triplet Sensitization of 9-vinylanthracene

To identify the triplet absorption spectrum of 9-vinyl anthracene (9VA) monomers, we performed a triplet sensitization experiment using platinum octaethylporphyrin (PtOEP). A mixture of 9VA and PtOEP in toluene was prepared and placed into a sealed cuvette. Photoexcitation of PtOEP's Q-band at 532 nm generates the lowest excited singlet state of PtOEP, which rapidly intersystem crosses to its triplet state on a ~165 fs timescale.[11] Since the energy of PtOEP's lowest triplet state is 1.9 eV,[12] which is higher than that of 9VA (~1.8 eV), diffusional collisions between photoexcited PtOEP and 9VA molecules can result in triplet energy transfer from PtOEP to 9VA, thus allowing us to identify 9VA's triplet absorption spectrum.

Supplementary Figure 5A plots TA spectra of solutions containing PtOEP and 9VA recorded following photoexcitation of PtOEP's Q-band. Immediately upon photoexcitation, features appear that match those seen in TA spectra PtOEP's T_1 state (**Supplementary Figure 5B**). Specifically, two photobleachs appear near 385 nm and 505 nm that are respectively attributed to PtOEP's Soret and the first vibrational replica of PtOEP's Q-band. A broad photoinduced absorption centered at 420 nm is also seen that associated with PtOEP's T_1 state. As time evolves, features associated with PtOEP's T_1 state decay, concomitant with the appearance of a sharp resonance peaked at 435 nm, which we assign to the T_1 state of 9VA monomers. This peak agrees well with prior reports of triplet spectra of 9MA[8] and other anthracene derivatives.[13–15]

Importantly, the absorption spectrum of the T_1 state of monomeric 9VA differs substantially from that of 9VA molecules that have been attached to the surface of Si QDs (**Figure 4B, main text**). We attribute

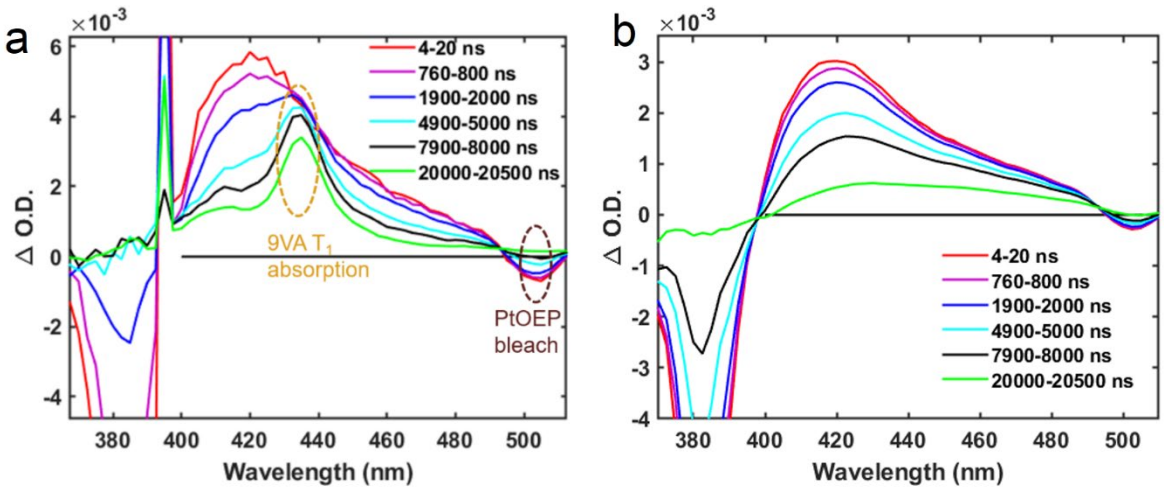

Supplementary Figure 5: (a) TA spectra of a PtOEP:9VA mixture excited at 532 nm. (b) TA spectra of PtOEP excited at 532 nm. The photobleaches that appear at 385 and 505 nm together with the broad induced absorption peaked at 420 nm are indicative of PtOEP's T_1 state.[11]

this difference to strong coupling of 9VA's triplet exciton state to those of the Si QD, which gives rise to a band of states with mixed QD:molecule character.

3.6. Transient Absorption Spectra of Si:9EA as a Function of $\langle N_{9EA} \rangle$

To assess if strong electronic coupling exists between Si QDs and 9EA molecules bound to their surface, TA experiments were performed on Si:9EA as a function of $\langle N_{9EA} \rangle$. **Supplementary Figure 6** plots TA spectra recorded 25 μs following excitation of Si:9EA at 532 nm. At this time delay, energy transfer from Si QDs to surface-bound 9EA molecules is fully complete, as evidenced by the appearance of a sharp resonance at 435 nm that corresponds to the $T_1 \rightarrow T_n$ absorption of surface-bound 9EA molecules.[8] Importantly, this band shows no change in its spectral position with increased loading of 9EA. This behavior is completely different from that shown by Si:9VA, which shows strong changes in its induced absorption spectra with changing 9VA surface concentration due to strong coupling between 9VA and silicon (**Figure 5B, main text**). The data in **Supplementary Figure 6** indicates that the sp^3 C-C bridge that connects Si to anthracene in Si:9EA gives rise to only weak electronic coupling between these materials.

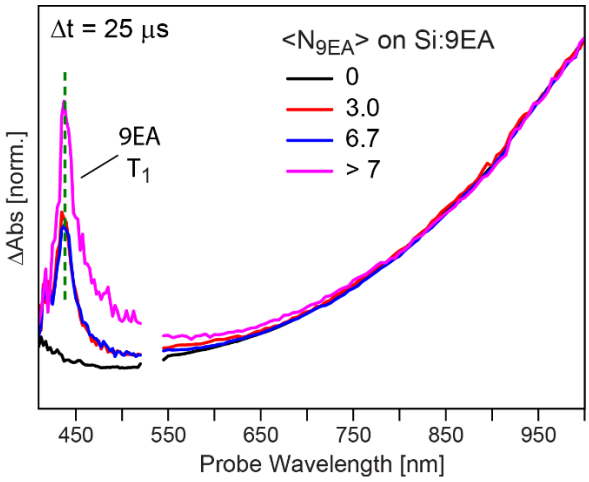

Supplementary Figure 6: TA spectra of Si:9EA as a function of 9EA surface concentration ($\langle N_{9EA} \rangle$ = 0, 2.98, 6.72, > 7). The $\langle N_{9EA} \rangle$ = 0 sample corresponds to Si:dodecane. Spectra were recorded 25 μs after excitation at 532 nm and are normalized to the Si QD induced absorption band at λ > 1000 nm.

3.7 Intersystem Crossing Timescale for Si:9VA

To determine the rate with which strongly-coupled triplet exciton states are populated following photoexcitation of Si:9VA, we employed a TA spectrometer with an instrument response function (IRF) of 1.6 ns. **Supplementary Figure 7** plots the rise of the induced absorption signal of the strongly-coupled triplet exciton state. A fit to this data reveals a growth timescale of 3 ns, which we attribute to intersystem crossing from the bright Si QD state that is responsible for light absorption to a spatially-delocalized Si:9VA triplet exciton state. We note that population of the spatially-delocalized triplet state of Si:9VA occurs faster than population of the weakly-coupled anthracene triplet state of Si:9EA, which was previously demonstrated to occur on a 15.2 ns timescale.[8]

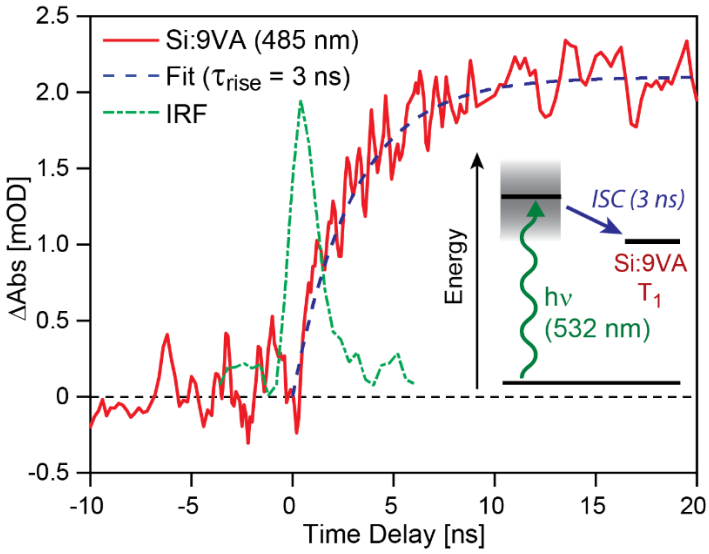

Supplementary Figure 7: TA kinetics of Si:9VA (red solid) measured at a probe wavelength of 485 nm following photoexcitation of Si:9VA at 532 nm. At this probe wavelength we observe development of a spectrally broad induced absorption band (**Figure 2A, main text**) that is attributed to a strongly-coupled triplet exciton state that spatially extends over both 9VA molecules and silicon. An exponential fit to the rise time of this band (blue dashed) yields a 3 ns time constant, that we attribute to the intersystem crossing timescale from the initial photoexcited Si QD state to the Si:9VA T_1 state (inset). This data was recorded using a nanosecond TA spectrometer with an instrument response function (IRF) of 1.6 ns (green dash dot).

3.8 Lifetime Comparison of Strongly-coupled and Weakly-coupled Triplet Exciton States

In the main text, we note that once optimized, the strongly-coupled Si:9VA system exhibits a higher upconversion quantum efficiency when paired with *t*Bu$_4$P compared to Si:9EA paired with DPA. To discern if these difference stem from a difference in the triplet exciton lifetime of these two Si QD systems, we have used TA to record the triplet exciton lifetime of each system. **Supplementary Figure 8** plots TA transients measured at a probe wavelength of 435 nm for Si:9EA and 480 nm for Si:9VA following photoexcitation at 532 nm. These wavelengths were selected as they selectively track induced absorption bands associated with weakly-coupled 9EA triplet excitons in Si:9EA and strongly-coupled triplet excitons in Si:9VA.

The decay of the induced absorption signal from each system does not follow a simple single exponential decay, but rather requires that a multiexponential decay fitting function be used to reproduce the measured dynamics (**Supplementary Table 3**). We have previously reported that the decay of Si QDs produced by a nonthermal plasma generally exhibit multiexponential relaxation kinetics,[5,12] which we attribute to a distribution of trap sites spread among QDs within a sample ensemble that facilitate nonradiative decay. Comparing the decay rates of Si:9VA and Si:9EA, we find Si:9VA decays slightly faster than Si:9EA. Over the 55 μs window we probe, the triplet exciton population of Si:9VA has decayed

by 73% while that of Si:9VA has decayed by 63%. This shorter lifetime suggests that the improved upconversion quantum efficiency we report for Si:9VA relative to Si:9EA does not stem from an extended lifetime for Si:9VA.

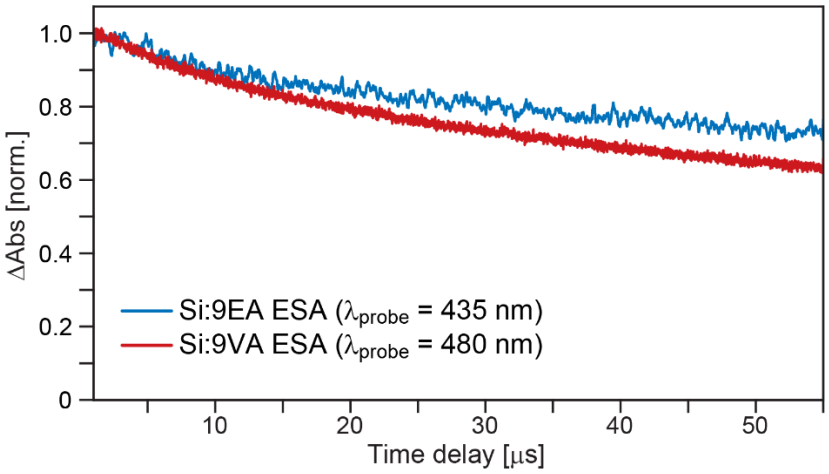

Supplementary Figure 8: TA kinetics and corresponding multiexponential fits of the triplet exciton excited state absorption of Si:9EA ($\langle N_{9EA} \rangle = 5.4$, $\lambda_{probe} = 435$ nm) and Si:9VA ($\langle N_{9EA} \rangle = 5.3$, $\lambda_{probe} = 480$ nm) measured following photoexcitation of each system at 532 nm.

	y_0	a_1	τ_1 [μs]	a_2	τ_2 [μs]	a_3	τ_3 [μs]
Si:9EA, λ_{probe} = 435 nm	0.343	0.056	3.32	0.171	22.1	0.438	234
Si:9VA, λ_{probe} = 480 nm	0.523	0.063	2.96	0.040	17.4	0.399	36.7

Supplementary Table 3: Parameters used to model the decay of the weakly-coupled triplet exciton state of Si:9EA and the strongly-coupled triplet exciton state of Si:9VA. Parameters were obtained by fitting TA transients obtained at a probe wavelength of 435 nm for Si:9EA and 480 nm for Si:9VA following photoexcitation of each system at 532 nm. Each decay transient was fit to a tri-exponential function plus offset: $\Delta Abs = y_0 + \sum_{n=1}^{3} a_n \exp(-t/\tau_n)$.

3.9 Potential for Anthracene Excimer Formation Following Si:9VA Excitation

While we have attributed the photoexcited dynamics we report for Si:9VA to intersystem crossing that populates a strongly-coupled triplet exciton state, pairs of anthracene molecules have been reported to form excimers upon photoexcitation. As we employ low surface concentrations of 9VA ($\langle N_{9VA} \rangle$ = < 2 to 7.3), it is unlikely that the majority of 9VA molecules that bind to a Si QD are colocalized on the surface, which is required for them to form either a ground-state aggregate or an excimer upon photoexcitation.

To additionally rule out excimer formation, we note that anthracene excimers are known to give rise to a broad emission band that extends from 460 – 650 nm.[16] **Supplementary Figure 9** plots emission spectra of Si:9VA particles that bind, on average, 5.9 9VA molecules per QD. This spectrum was recorded by exciting the system at 375 nm wherein both 9VA and Si directly absorb light. We observe two emission bands, one peaked at 440 nm that can be attributed to emission from the 9VA S_1 state, and a second peaked near 785 nm that arises from Si QD excitons. We observe no distinct emission band between 460 to 650 nm, indicating that anthracene excimer formation is not a dominant relaxation pathway in Si:9VA.

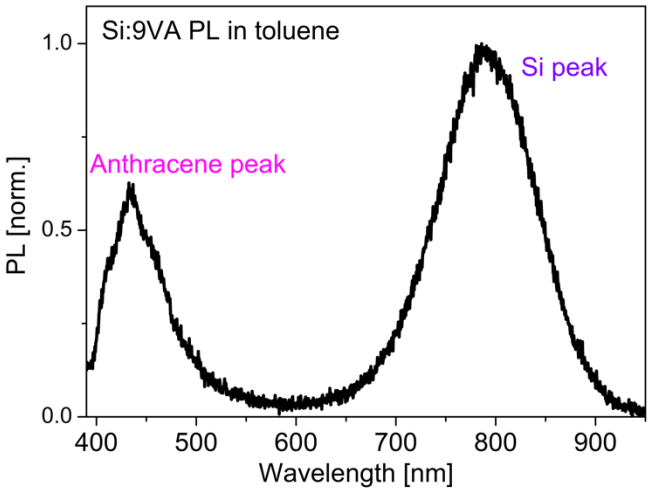

Supplementary Figure 9: Emission spectra of Si:9VA ($\langle N_{9VA} \rangle$ = 5.9) in toluene (λ_{Ex} = 375 nm).

3.10 Additional Control Photon Upconversion Measurements

In **Figure 2B** of the main text, we compare the ability of Si:9VA particles with a high 9VA surface loading ($\langle N_{9VA} \rangle > 7$) to produce upconverted emission from DPA and *t*Bu$_4$P. We find the UCQY produced when Si:9VA is paired with *t*Bu$_4$P is substantially higher than when it is paired with DPA (2.7% vs. 0.03%). We attribute the improved performance with *t*Bu$_4$P to a lowering of Si:9VA's triplet exciton energy due to strong coupling between Si QDs and 9VA molecules. By reducing the 9VA surface concentration of these particles, we can increase their upconversion efficiency when paired with *t*Bu$_4$P to 17.2% (**Figure 5D, main text**). We ascribe this behavior to raising of the Si:9VA triplet exciton energy to better match that of *t*Bu$_4$P.

While we can tune the triplet exciton energy of strongly-coupled systems such as Si:9VA by changing the number of transmitter molecules they bind, such tuning should not be possible in weakly-coupled systems such as Si:9EA. To test this, we have carried out a control experiment wherein we have paired Si:9EA particles that feature a high surface concentration of 9EA ($\langle N_{9EA} \rangle > 7$) with both DPA and *t*Bu$_4$P. As Si:9EA is a weakly-coupled system, as we increase 9EA surface concentration, the triplet exciton energy of transmitter molecules should not change. As 9EA possesses a high triplet energy (~1.79 eV), we expect it should function as a suitable energy donor for both DPA and *t*Bu$_4$P. Upconversion spectra measured for these two systems are plotted in **Supplementary Figure 10**. At this high concentration, we find Si:9EA

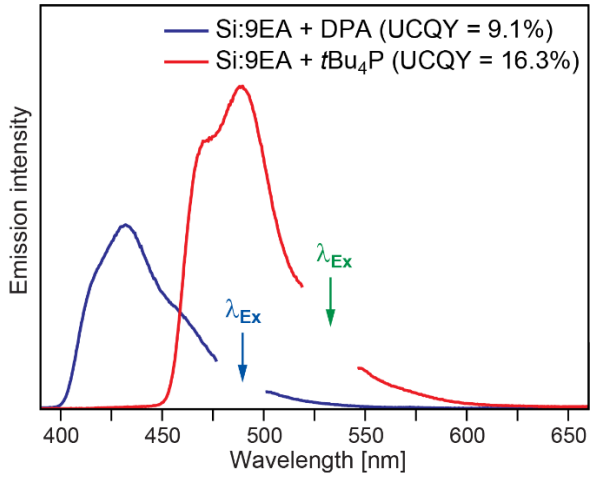

Supplementary Figure 10: Emission spectra of mixtures of Si:9EA ($\langle N_{9EA} \rangle > 7$) with DPA (5.2 mM, blue, λ_{Ex} = 488 nm) and *t*Bu$_4$P (5.2 mM, red, λ_{Ex} = 532 nm).

indeed functions well as a sensitizer for both emitters, achieving UCQYs of 9.1% and 16.3% for DPA and *t*Bu$_4$P, respectively.

In addition to the control experiment above, we have also verified that surface-bound anthracene molecules are indeed crucial to achieving photon upconversion by performing measurements on Si:dodecane particles that have been paired with DPA molecules in solution. **Supplementary Figure 11** plots emission spectra of this system. When photoexcited, we find that the majority of the observed emission stems from Si:dodecane, with only a minor contribution from upconverted emission produced by DPA. Quantifying the intensity of this emission, we find that the UCQY is only a paltry 0.18%. This highlights that surface-bound anthracene molecules are needed to transmit triplet excitons to molecules diffusing in solution. In the absence of these molecules, the dodecane shell that surrounds a Si QD acts as an effective tunneling barrier that prevents triplet exciton transfer.

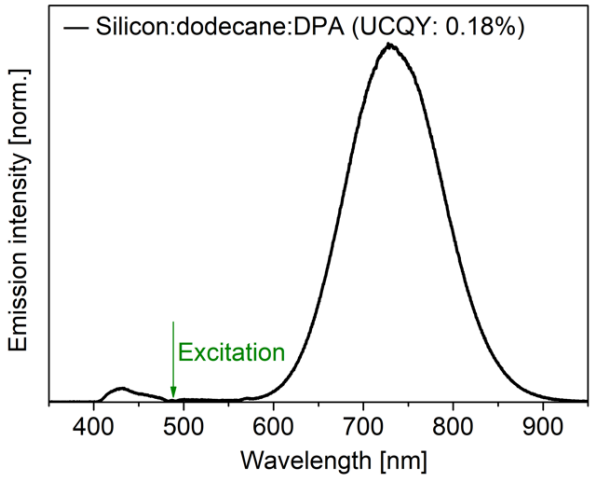

Supplementary Figure 11: Emission spectra of a toluene solution containing Si:dodecane particles and 5 mM DPA. Only a meager amount of upconverted emission is seen, which highlights that anthracene ligands are needed to transmit energy from a Si QD to DPA molecules in solution.

4. Computational Methods

4.1. Silicon Model

For the computational modeling of the electronic structures of Si:9VA and Si:9EA, we employed a surface slab model consisting of six crystalline silicon layers terminated with Si(111) facets. Our slab model is semiperiodic: non-periodic in the surface normal-direction (z-axis), but periodically replicated along the plane that contains the terminating facets (x–y plane). Silicon's (111) facet was selected for computational modeling due to its stability relative to other silicon facets.[17–20] Si(111) also has each of its surface bonds oriented along the surface-normal direction, facilitating attachment of a single 9VA or 9EA molecule to the slab. All other silicon dangling bonds were passivated with hydrogen atoms. In the absence of any molecular attachments to silicon, this model yields two equivalent surface layers, each with 16 attachment sites, which corresponds to a 4×4 supercell expansion of the primitive Si(111) surface unit cell. This surface arrangement corresponds to a hexagonal cell, with equal in-plane lattice constants of 15.33 Å (**Supplementary Figure 12**).

For a nonpolar hydrocarbon like 9VA or 9EA, we expect spurious interactions between molecules in periodic images to be small. We choose to put only a single 9VA or 9EA molecule on one of the slab's two surfaces—rather than one molecule on both surfaces—as the geometry of these molecules when attached to silicon is computationally expensive to converge. We leave the bottom 2 layers of silicon atoms frozen in their bulk positions during all geometry relaxations, and we relax all other atoms to a force convergence of less than 10 meV/Å.

We use density functional theory (DFT) computed with the Vienna Ab initio Simulation Package

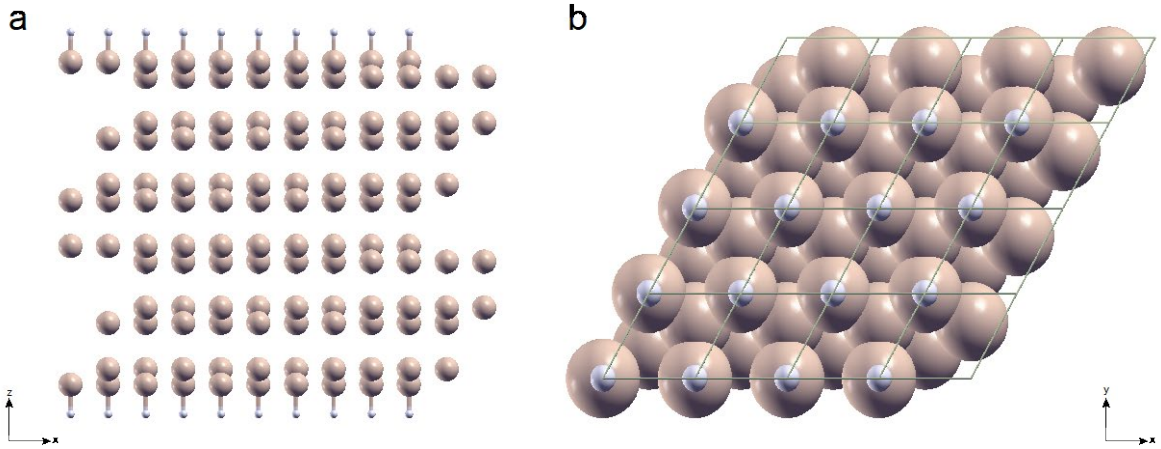

Supplementary Figure 12: Surface slab supercell with no molecular attachments. (a) Side view of the surface slab supercell. Silicon atoms are tan and hydrogen atoms, which passivate the top-most layer of silicon, are gray. We do not show bonds between silicon atoms and only show the Si-H bonds at each surface so that the surface layers are distinct from the interior layers. Layers of silicon stacked in the z-direction are separated by whitespace, yielding 6 layers in total. (b) Top-down view of the surface slab supercell. We illustrate the atoms as space-filling spheres in this view so that the stacking of atoms below the surface layer is more obvious. The individual unit cell divisions are shown with small rhombuses, 16 in total, corresponding to a 4×4 supercell expansion, with the surface layer parallel to the x–y plane. The in-plane lattice constants are the same and equal to 15.33 Å. A molecular attachment can replace any hydrogen atom on either surface. We choose to attach 9VA or 9EA to the top-most surface when simulating the full Si:9VA or Si:9EA systems, respectively, thus generating an asymmetric slab model.

(VASP)[21–24] to interrogate the electronic structure of Si:9VA and Si:9EA. These calculations employ the projector augmented wave (PAW) method for the atomic potentials and the Perdew-Burke-Ernzerhof (PBE) generalized gradient approximation for the exchange–correlation functional.[25,26] Hydrocarbon molecules and silicon have similar electronegativities, and as a result, the dispersion interaction can be important. However, bare DFT does not usually describe those interactions well. As such, we apply dispersion corrections to the PBE forces and energy using the DFT-D3(BJ) correction method of Grimme at al.[27,28] The PAW-PBE-D3(BJ) potential, in combination with a 540 eV plane-wave kinetic energy cutoff, yields a bulk silicon lattice constant of 5.42 Å, which is only a picometer smaller than experiment (5.43 Å).[29] To compute the triplet states in the slab calculations, we allow spin-polarization and force the calculation to find the lowest-energy triplet configuration, with a total spin component of $\pm\hbar$. These two spin components correspond to up and down spin channels, respectively.

4.2. Assessing Silicon:Molecule Coupling via the Density of States

The density of states (DOS) is the quantitative tool that we use to assess coupling between the electronic states of silicon and both 9VA and 9EA. The DOS is proportional to the trace of the imaginary part of the retarded Green's function:

$$G(E) = \frac{1}{E - H + i\varepsilon} \tag{3}$$

where ε is a small positive number that formally approaches zero from the right. The molecule-solid Hamiltonian is:

$$H = H_{mol} + H_{solid} + V \equiv H_0 + V, \tag{4}$$

where V is the coupling. When $V = 0$, the Green's function is a sum over poles that have resonances at the

energies of the uncoupled molecule and solid. A nonzero coupling causes deviations from this form, and those deviations are related to the self-energy that characterizes the molecule-solid interaction.[30,31] In particular, for an eigenstate $|j\rangle$ of the molecular Hamiltonian, H_{mol}, one can define:

$$G_{jj}(E) = \langle j| \frac{1}{E - H + i\varepsilon} |j\rangle \tag{4}$$

and the projected density of states (PDOS):

$$D_j(E) = -\frac{Im\left[G_{jj}(E)\right]}{\pi} = \sum_{\alpha=1}^{N} |\langle j|\alpha\rangle|^2 \delta(E - E_\alpha) \tag{5}$$

where $H|\alpha\rangle = E_\alpha|\alpha\rangle$. When the coupling vanishes, $|\langle j|\alpha\rangle|^2 = \delta_{j=\alpha}$ and the PDOS has one and only one peak at the energy ϵ_j of the molecule. However, when there is coupling, this single resonance will shift and broaden—an effect quantified by the self-energy of the Fano-Anderson model,[30,31] but observable in the PDOS. Because it is prohibitively expensive to localize all relevant states of the molecule and the solid, as we have done in the past for the related problem of hole diffusion on the surfaces of semiconducting nanocrystals,[32–34] it is more convenient to analyze the PDOS than it is to compute the self-energy.

Supplementary Figure 13 highlights the DOS computed for Si:9VA and Si:9EA, which is summed over both spin-up and spin-down triplet channels. Note that due to our use of spin-unrestricted DFT, these DOS correspond to the effective single-particle orbitals for electrons and holes that, when paired, give rise to a triplet exciton configuration. The energy axis for both Si:9VA and Si:9EA is set such that the valence band edge corresponds to the zero of energy. States with energy below this value correspond to excited hole states within the valence band while those with energies above this value correspond to excited electron states within the conduction band. We compute the exciton DOS shown in **Figure 3A** of the main text by convolving the DOS for these two bands to give rise to triplet exciton configurations. We can show this by starting with the definition of the exciton DOS:

$$D_{ex}(E) = \sum_e \sum_h \delta(E - (\varepsilon_e - \varepsilon_h)) \tag{6}$$

where ε_e and ε_h are the electron and hole energies, respectively. Using elementary properties of the delta function, we find:

$$D_{ex}(E) = \int dE' \sum_e \delta(E' + E - \varepsilon_e) \sum_h \delta(E' - \varepsilon_h) \tag{7}$$

or equivalently

$$D_{ex}(E) = \int dE' \rho_e(E' + E)\rho_h(E') \tag{8}$$

where $\rho_{e/h}(E) = \sum_{e/h} \delta(E - \varepsilon_{e/h})$ is the DOS for the electrons/holes in the conduction/valence band.

Supplementary Figure 13 also shows the PDOS computed for the carbon p-orbitals of each system. We use these orbitals as surrogates for the frontier molecular orbitals (HOMO and LUMO) that would comprise the eigenstates of the isolated molecule. This is not a particularly accurate approximation, but the inaccuracies in making it are identical for 9VA as they are for 9EA, which allows us to infer differences in the coupling of these two materials to silicon by comparing their carbon p-orbital PDOS. As with the exciton density of states shown in **Figure 3A** of the main text, we calculate the exciton PDOS shown in that same figure by convolving the PDOS computed for the valence and conduction bands shown in **Supplementary Figure 13**.

Examining the PDOS for Si:9EA, we find that these peaks are very narrow in energy, which is what we expect to see in the case wherein V is small. This energy localization indicates minimal mixing between

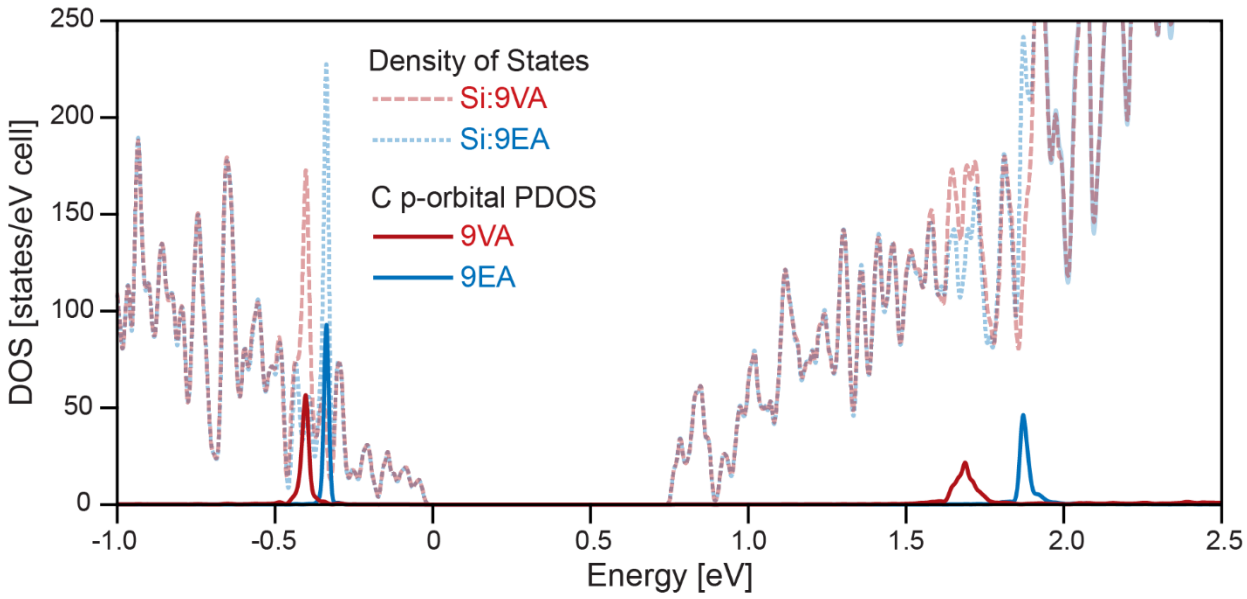

Supplementary Figure 13: (A) Density of states (DOS) computed for Si:9VA (light red dashed) and Si:9EA (light blue dotted). Projected contributions to these states from the carbon p-orbitals of 9VA and 9EA are plotted as solid red and blue lines, respectively (carbon atom p-orbital, projected density of states: PDOS). These projections identify adiabatic states that contain contributions from the frontier orbitals (HOMO and LUMO) of these molecules. We set the valence band maximum as the zero of energy. The carbon p-orbital PDOS between -0.5 and 0 eV corresponds to a molecular HOMO peak, while the carbon p-orbital PDOS between 1.5 and 2 eV corresponds to a molecular LUMO peak. We note that the total DOS for each system is nearly identical, except in the vicinity of the HOMO and LUMO PDOS contributions to the total DOS.

the molecular orbitals of 9EA with those of silicon. In contrast, the PDOS of Si:9VA show significant energetic broadening, indicating that the valence orbitals of 9VA hybridize with several silicon states. This gives rise to new, strongly-coupled triplet exciton states wherein charge carriers straddle the silicon:9VA interface, as visualized in **Figure 3C** of the main text.

4.3. Calculation of Partial Charge Densities

To aid in interpreting the computed DOS for Si:9VA and Si:9EA (**Figures 3A, main text** & **Supplementary Figure 13**), we calculate the partial charge densities near the carbon p-orbital PDOS maxima to assess the electronic coupling between silicon and surface-bound anthracene molecules. These partial charge densities reveal the orbital density within a user-specified energy range, which allows us to visualize the degree to which these orbitals spatially extend over both the silicon lattice and anthracene molecules anchored to it.

Figures 3B & **3C** of the main text highlight the partial charge densities computed by examining a range of states whose energies fall within the peaks of the carbon p-orbital PDOS within the valence bands of Si:9VA and Si:9EA. We choose to focus on states in the valence band, which are constructed in part from the HOMOs of 9VA and 9EA, as they are occupied in the DFT calculation, which aids their computed accuracy. We note that the calculation of partial charge densities can be subject to user bias due to the need to define an energy range over which these densities are summed. For example, if molecules bound to the surface of silicon were completely uncoupled to it, one could obtain charge density plots that showed density spread across the silicon:molecule interface simply by choosing an energy integration range that was large enough to encompass the uncoupled states of both systems. Hence, our choice to examine states within the valence band rather than the conduction band of each system is also motivated by the lower total DOS near the peaks of the carbon p-orbital PDOS in the valence band. This makes a partial charge density

analysis less prone to contamination by energetically close-lying silicon states that are not necessarily coupled to either 9VA or 9EA.

The partial charge density plots in **Figures 3B** & **3C** of the main text were constructed by summing the charge densities of states within the full-width at half-max (FWHM) of the carbon p-orbital PDOS peaks in the valence band for Si:9VA and Si:9EA. The FWHM corresponds to an energy range of 24.7 meV and 17.9 meV, respectively. These charge densities correspond to the spatial extent of the hole contribution to the triplet exciton states formed by 9VA and 9EA in each system. Examining these densities, we find that while the triplet exciton states remain spatially localized to 9EA, they spatially extend across the silicon|9VA interface, indicating the presence of weak electronic coupling in Si:9EA and strong electronic coupling in Si:9VA.

The use of a consistent integration range for both Si:9VA and Si:9EA should reduce the possibility that the difference in the charge density plots shown in **Figures 3B** & **3C** of the main text result not from the presence of strong coupling in Si:9VA, but rather from the inclusion of spurious uncoupled silicon states that happen to fall in the energy integration range. In choosing the FWHM for these two systems, we find that despite the difference in the energy ranges that generated the partial charge densities, the same number of eigenstates reside within each range: 20 eigenstates for each system in the first Brillouin zone, or 11 states in the irreducible Brillouin zone where the symmetry $\Psi_{\boldsymbol{k}} = \Psi^{*}_{-\boldsymbol{k}}$ is considered. We note that the former value across the full first Brillouin zone is more meaningful for this analysis; however, we mention both quantities since VASP only calculates the states within the irreducible Brillouin zone, along with their corresponding weights due to the aforementioned k-point symmetry.

We construct the FWHM partial charge density plots according to the wavefunctions of each system before calculating the DOS. We first calculate these wavefunctions self-consistently on a Γ-centered 3×3×1 k-point grid. Using the total charge density corresponding to these wavefunctions as inputs, we then calculate the subsequent DOS plots non-self-consistently on a Γ-centered 9×9×1 k-point grid. This allows us to define a FWHM of the relevant PDOS peaks in either system. The parent 3×3×1 k-point grid converges the total energy of the system to approximately 0.1 meV/atom, which ensures an accurate charge density. The 20 eigenstates within the FWHM of each system's carbon p-orbital PDOS in the valence band reside on the 3×3×1 k-point grid.

References

(1) Nierth, A.; Kobitski, A. Yu.; Nienhaus, G. U.; Jäschke, A. Anthracene−BODIPY Dyads as Fluorescent Sensors for Biocatalytic Diels−Alder Reactions. *J. Am. Chem. Soc.* **2010**, *132* (8), 2646–2654.

(2) Anthony, R. J.; Cheng, K.-Y.; Holman, Z. C.; Holmes, R. J.; Kortshagen, U. R. An All-Gas-Phase Approach for the Fabrication of Silicon Nanocrystal Light-Emitting Devices. *Nano Lett.* **2012**, *12* (6), 2822–2825.

(3) Li, Z.; Kortshagen, U. R. Aerosol-Phase Synthesis and Processing of Luminescent Silicon Nanocrystals. *Chem. Mater.* **2019**, *31* (20), 8451–8458.

(4) Mangolini, L.; Thimsen, E.; Kortshagen, U. High-Yield Plasma Synthesis of Luminescent Silicon Nanocrystals. *Nano Lett.* **2005**, *5* (4), 655–659.

(5) Wheeler, L. M.; Anderson, N. C.; Palomaki, P. K. B.; Blackburn, J. L.; Johnson, J. C.; Neale, N. R. Silyl Radical Abstraction in the Functionalization of Plasma-Synthesized Silicon Nanocrystals. *Chem. Mater.* **2015**, *27* (19), 6869–6878.

(6) Huang, T.; Koh, T. T.; Schwan, J.; Tran, T. T.-T.; Xia, P.; Wang, K.; Mangolini, L.; Tang, M. L.; Roberts, S. T. Bidirectional Triplet Exciton Transfer between Silicon Nanocrystals and Perylene. *Chem. Sci.* **2021**, *12* (19), 6737–6746.

(7) Carroll, G. M.; Limpens, R.; Neale, N. R. Tuning Confinement in Colloidal Silicon Nanocrystals with Saturated Surface Ligands. *Nano Lett.* **2018**, *18* (5), 3118–3124.

(8) Xia, P.; Raulerson, E. K.; Coleman, D.; Gerke, C. S.; Mangolini, L.; Tang, M. L.; Roberts, S. T. Achieving Spin-Triplet Exciton Transfer between Silicon and Molecular Acceptors for Photon Upconversion. *Nat. Chem.* **2020**, *12* (2), 137–144.

(9) Olesund, A.; Johnsson, J.; Edhborg, F.; Ghasemi, S.; Moth-Poulsen, K.; Albinsson, B. Approaching the Spin-Statistical Limit in Visible-to-Ultraviolet Photon Upconversion. *J. Am. Chem. Soc.* **2022**, *144* (8), 3706–3716.

(10) Haefele, A.; Blumhoff, J.; Khnayzer, R. S.; Castellano, F. N. Getting to the (Square) Root of the Problem: How to Make Noncoherent Pumped Upconversion Linear. *J. Phys. Chem. Lett.* **2012**, *3* (3), 299–303.

(11) Roberts, S. T.; Schlenker, C. W.; Barlier, V.; McAnally, R. E.; Zhang, Y.; Mastron, J. N.; Thompson, M. E.; Bradforth, S. E. Observation of Triplet Exciton Formation in a Platinum-Sensitized Organic Photovoltaic Device. *J. Phys. Chem. Lett.* **2011**, *2*, 48–54.

(12) Baldo, M. A.; O'Brien, D. F.; You, Y.; Shoustikov, A.; Sibley, S.; Thompson, M. E.; Forrest, S. R. Highly Efficient Phosphorescent Emission from Organic Electroluminescent Devices. *Nature* **1998**, *395*, 151–154.

(13) Craig, D. P.; Ross, I. G. The Triplet–Triplet Absorption Spectra of Some Aromatic Hydrocarbons and Related Substances. *J Chem Soc* **1954**, 1589–1606.

(14) Chattopadhyay, S. K.; Kumar, Ch. V.; Das, P. K. Triplet-Related Photophysics of 9.10-Diphenylanthracene. A Kinetics Study of Reversible Energy Transfer from Anthracene Triplet by Nanosecond Laser Flash Photolysis. *Chem. Phys. Lett.* **1983**, *98* (3), 250–254.

(15) Carmichael, I.; Hug, G. L. Triplet–Triplet Absorption Spectra of Organic Molecules in Condensed Phases. *J. Phys. Chem. Ref. Data* **1986**, *15* (1), 1–250.

(16) Das, A.; Danao, A.; Banerjee, S.; Raj, A. M.; Sharma, G.; Prabhakar, R.; Srinivasan, V.; Ramamurthy, V.; Sen, P. Dynamics of Anthracene Excimer Formation within a Water-Soluble Nanocavity at Room Temperature. *J. Am. Chem. Soc.* **2021**, *143* (4), 2025–2036.

(17) Follstaedt, D. M. Relative Free Energies of Si Surfaces. *Appl. Phys. Lett.* **1993**, *62* (10), 1116–1118.

(18) Jaccodine, R. J. Surface Energy of Germanium and Silicon. *J. Electrochem. Soc.* **1963**, *110* (6), 524.

(19) Eaglesham, D. J.; White, A. E.; Feldman, L. C.; Moriya, N.; Jacobson, D. C. Equilibrium Shape of Si. *Phys. Rev. Lett.* **1993**, *70* (11), 1643–1646.

(20) Lu, G.-H.; Huang, M.; Cuma, M.; Liu, F. Relative Stability of Si Surfaces: A First-Principles Study. *Surf. Sci.* **2005**, *588* (1–3), 61–70.

(21) Kresse, G.; Hafner, J. Ab Initio Molecular Dynamics for Liquid Metals. *Phys. Rev. B* **1993**, *47* (1), 558–561.

(22) Kresse, G.; Hafner, J. *Ab Initio* Molecular-Dynamics Simulation of the Liquid-Metal–Amorphous-Semiconductor Transition in Germanium. *Phys. Rev. B* **1994**, *49* (20), 14251–14269.

(23) Kresse, G.; Furthmüller, J. Efficiency of Ab-Initio Total Energy Calculations for Metals and Semiconductors Using a Plane-Wave Basis Set. *Comput. Mater. Sci.* **1996**, *6* (1), 15–50.

(24) Kresse, G.; Furthmüller, J. Efficient Iterative Schemes for *Ab Initio* Total-Energy Calculations Using a Plane-Wave Basis Set. *Phys. Rev. B* **1996**, *54* (16), 11169–11186.

(25) Blöchl, P. E. Projector Augmented-Wave Method. *Phys. Rev. B* **1994**, *50* (24), 17953–17979.

(26) Kresse, G.; Joubert, D. From Ultrasoft Pseudopotentials to the Projector Augmented-Wave Method. *Phys. Rev. B* **1999**, *59* (3), 1758–1775.

(27) Grimme, S.; Antony, J.; Ehrlich, S.; Krieg, H. A Consistent and Accurate *Ab Initio* Parametrization of Density Functional Dispersion Correction (DFT-D) for the 94 Elements H-Pu. *J. Chem. Phys.* **2010**, *132* (15), 154104.

(28) Grimme, S.; Ehrlich, S.; Goerigk, L. Effect of the Damping Function in Dispersion Corrected Density Functional Theory. *J. Comput. Chem.* **2011**, *32* (7), 1456–1465.

(29) Kittel, C. *Introduction to Solid State Physics*; John Wiley and Sons: New York, 1976.

(30) Mukamel, S. *Principles of Nonlinear Optical Spectroscopy*; Oxford University Press: New York, 1995.

(31) Mahan, G. D. *Many-Particle Physics*, 3rd ed.; Springer: New York, NY, 2000.

(32) Cline, R. P.; Utterback, J. K.; Strong, S. E.; Dukovic, G.; Eaves, J. D. On the Nature of Trapped-Hole States in CdS Nanocrystals and the Mechanism of Their Diffusion. *J. Phys. Chem. Lett.* **2018**, *9* (12), 3532–3537.

(33) Cline, R. P.; Eaves, J. D. Surface-Trapped Hole Diffusion in CdS and CdSe: The Superexchange Mechanism. *J. Phys. Chem. C* **2020**, *124* (51), 28244–28251.

(34) Utterback, J. K.; Cline, R. P.; Shulenberger, K. E.; Eaves, J. D.; Dukovic, G. The Motion of Trapped Holes on Nanocrystal Surfaces. *J. Phys. Chem. Lett.* **2020**, *11* (22), 9876–9885.